Synthesis and Characterization of Carbon Nanotube-Doped Thermoplastic Nanocomposites for the Additive Manufacturing of Self-Sensing Piezoresistive Materials

Citation: Verma, Pawan, Ubaid, Jabir, Varadarajan, Kartik M, Wardle, Brian L and Kumar, S. 2022. "Synthesis and Characterization of Carbon Nanotube-Doped Thermoplastic Nanocomposites for the Additive Manufacturing of Self-Sensing Piezoresistive Materials." ACS Applied Materials & Interfaces, 14 (6).

Published Version: 10.1021/ACSAMI.1C20491

Publisher: American Chemical Society (ACS)

Permanent Link: https://hdl.handle.net/1721.1/145648

Version: Author's final manuscript: final author's manuscript post peer review, without publisher's formatting or copy editing

Synthesis and characterization of carbon nanotube doped thermoplastic nanocomposites for the additive manufacturing of self-sensing piezoresistive materials

*Pawan Verma, Jabir Ubaid, Kartik M Varadarajan, Brian L Wardle and S. Kumar**

Dr. Pawan Verma,
Artie McFerrin Department of Chemical Engineering, Texas A&M University, College Station, TX, 77840, USA.

Dr. Jabir Ubaid, Prof S. Kumar
James Watt School of Engineering, University of Glasgow, Glasgow, G12 8LT, UK
E-mail*: s.kumar@eng.oxon.org

Prof. Kartik M. Varadarajan
Department of Orthopedic Surgery, Massachusetts General Hospital, Boston, MA 02114, USA

Prof. Brian L. Wardle
Department of Aeronautics and Astronautics, Massachusetts Institute of Technology, Cambridge, MA 02139, USA
Department of Mechanical Engineering, Massachusetts Institute of Technology, Cambridge, MA 02139, USA

Keywords: Melt-blending, additive manufacturing, piezoresistivity, self-sensing, orthopaedic braces

Abstract

We present carbon nanotube (CNT) reinforced polypropylene random copolymer (PPR) nanocomposites for additive manufacturing of self-sensing lattice structures via fused filament fabrication. The PPR/CNT feedstock filaments were synthesized through high shear-induced melt-blending with controlled CNT loading up to 8 wt.% to enable 3D printing of nanoengineered PPR/CNT architected structures. The CNTs were found to enhance crystallinity (up to 6%) in the PPR printed parts, contributing to the overall CNT-reinforcement effect that increases both stiffness and strength (increases of 56% in modulus and 40% in strength at 8 wt.% CNT loading). Due to electrical conductivity (~10^{-4} -10^{-1} S/cm with CNT loading) imparted to the PPR by the CNT network, multifunctional *in situ* strain and damage sensing in 3D-printed CNT/PPR bulk

composites and lattice structures is revealed. A useful range of gauge factors (k) is identified for strain-sensing ($k_s = 10.1 - 17.4$) and damage-sensing ($k_d = 20 - 410$) across the range of CNT loadings for the 0^o print direction. Novel auxetic re-entrant and S-unit cell lattices are printed, with multifunctionality demonstrated as strain- and damage-sensing in tension. The PPR/CNT multifunctional nanocomposite lattices demonstrated here exhibit tuneable strain- and damage-sensitivity and have application in biomedical engineering for the creation of self-sensing patient-specific applications such as orthopaedic braces, where the ability to sense strain (and stress) can provide direct information for optimization of brace design/fit over the course of treatment.

Introduction

Additive manufacturing (AM), also known as 3D printing, is a revolutionary technology for the efficient manufacturing of geometries which can't be produced by conventional techniques [1, 2, 3]. AM delivers freedom of design, mass customization, waste minimization and fast prototyping along with low processing cost [1, 2, 4, 56]. Fused filament fabrication (FFF, sometimes called fused deposition molding, or FDM™) has emerged as an attractive AM technology due to its simplicity and reproducibility at relatively low cost [2, 7, 8] as compared to other common AM processes. FFF usually utilizes continuous filaments of thermoplastic polymer or polymer blends or polymer composites to create structures via a heated print head that meltbonds the filaments to each other. Commodity polymers such as polypropylene (PP) and its copolymers can be easily processed via FFF process, as PP exhibits a wide processing window [8, 9 10]. Although, PP is a lightweight, low-cost thermoplastic material, its mechanical properties are not exceptional. Several studies focused on modifying PP to improve their mechanical performance utilizing different micro or nano fillers. AM of polymers reinforced with micro-fibres and -particles, and increasingly nano-fibres and -particles, is a route towards enhanced mechanical performance as well as multifunctionality [11, 12]

[13]. In the last two decades, much work on bulk polymer nanocomposites (PNCs) reinforced with conductive fillers such as metal nanoparticles, graphene, and carbon nanotubes (CNTs), have been pursued to both enhance mechanical properties and impart multifunctionality [14, 15]. A major focus continues to be on carbon nanostructures (CNS), including CNTs, graphene, carbon nanofibers, and other allotropes of carbon [12, 16]. Extant work on processing CNS in polymers has shown that the CNS can impart changes to the polymer due to several mechanisms, with stronger effects generally noted for thermoplastics, principally via enhancement of crystallinity. Further, while mechanical property enhancement has had mixed results [17], electrical conductivity modification via the percolation mechanism is extremely effective at converting the insulating polymer into an electrically conductive material at very low loadings (wt.% or vol.%) of CNS [14, 18, 19]. CNTs exhibit excellent strength (~10-100 GPa), modulus (~1.0 TPa), electrical conductivity (10^4-10^6 S/cm) and thermal conductivity (3000-6000 W/m K), evidencing their superiority over other allotropes of carbon [5, 20]. As a result, CNT reinforced polymers have emerged as the most promising advanced material for making FFF filaments because of their exceptional intrinsic properties and processibility of relatively long (mm-scale) nanofibers in the continuous FFF filaments [17]. This allows for low loadings of CNTs to create percolation and provide electrical conductivity which is useful for, among others, sensor applications based on piezoresistivity of the CNT network [18, 21, 22]. Piezoresistive strain and damage sensing are the most-studied multifunctionality in polymer nanocomposites to date, with a recent review separating out strain sensing which is best quantified via a gauge factor (the slope of relative change in resistance versus strain curve) in the linear elastic regime, and in the hysteretic (plasticity and damage are the dominant mechanisms) regime for bulk materials [21]. Reported gauge factors for such materials are noted to be in the useful range for sensing, similar to the gauge factors ($k = 0.6$ to 10) of commercial strain sensors[23]. Bulk PP/CNT

nanocomposites, of direct interest here, have been reported with similar gauge factors [24]. The extant literature confirms that piezoresistive sensors based on conductive CNS in polymers offer numerous possible applications such as health and fitness monitoring, prosthetic device tailoring and monitoring, soft robotic sensing, and human-machine interface solutions such as skin-mountable motion sensors, among others [4, 25]. One particularly interesting example in patient-specific biomedical devices for FFF-printed piezoresistive PP lattice designs is orthopaedic bracing, such as those used for scoliosis deformity correction. Currently, these braces are made from PP by conventional machining and moulding approaches and fit to the needs of individual patients manually via trial and error [26]. Furthermore, there is no information available to ensure that the appropriate amount of stress is being transmitted to the spine in different directions, or to direct the timing of any necessary adjustments such as to account for growth of the paediatric patients, leaving fitting and adjustment of fixed scoliosis bracing as more of an art than science. A smart 3D printed brace comprised of a piezoresistive material would offer the ability to sense stress in brace elements and provide information to tune the stiffness of the bracing in different directions, time brace adjustments based in patient-specific data, and (enabled via AM), to print new braces or brace elements as the patient's progress advances. This has tremendous potential via a virtuous cycle of smart sensing and adjustment to improve the outcomes of over 30,000 children fitted with a scoliosis brace each year, and the 38,000 children undergoing surgical intervention each year in the US alone to address progressive deformities not adequately addressed via inefficient methods such as current bracing [27].

We study polypropylene random copolymer (PPR) which offers (vs. PP) processing and economic advantage, due to comparative cost, improved mechanical properties and low (20–30°C less) processing temperature, making it energetically economical. PPR has lower glass transition

temperature and melting temperature (compared to PP) which also means the part softens earlier when heated but will also reduce any warping caused during printing since the part will finish cooling before solidifying, matching well to FFF AM needs [28]. Focusing on the FFF of PPR/CNT materials, both the mechanical property changes of the bulk material, as well as piezoresistive multifunctionality is quantified, in addition to demonstration of novel auxetic self-sensing 2D lattice structures (see Figure 1). The effect of CNT content (wt.% loading of CNTs) on the electrical conductivity, mechanical properties and piezoresistive behaviour was determined via comparison to neat PPR printed on the same machine. The obtained results confirm the formation of conductive network even at very low CNTs loading (~1.40 wt.%) in the printed PPR matrix, with tuneable gage factors in the linear and hysteretic regimes that are similar to those observed in bulk polymer-CNS studies. Since nearly all biomedical applications require performance over cyclic loading, for instance the prosthetic and brace structures, cyclic performance is also quantified for the FFF-printed PPR/CNT structures. This study can be used to inform FFF manufacturing of PPR/CNT nanocomposite structures with tuneable strain and damage sensing multifunctionality for a variety of biomedical applications such as next generation smart orthopaedic braces.

Materials and Methods

PPR (RA140E procured from Borouge Pte. Ltd) having a melt flow index of 0.3g/10 min (testing temperature 230 ^{o}C with 2.16kg mass; tested as per ASTM 1238 [29]) was used as a matrix. The melting and crystallization temperatures of the FFF-printed PPR were observed to be 147.7 ^{o}C and 112.2 ^{o}C, respectively, with a crystallinity of 30.8 wt.% via DSC (see discussion in section S2 and Tables S1 and S2). The carbon nanostructures (CNS) studied here, comprise clusters of aligned multi-walled carbon nanotubes (MWCNTs) with a high degree of entanglement [30]. They were

supplied by Applied Nanostructured Solution, LLC. The CNS were grown via chemical vapour deposition (CVD) on glass microfibre substrates [31]. The average outer diameter of the CNTs is in the range of ~10-12 nm and length >30 μm, while purity of MWCNTs determined from thermogravimetric analysis (TGA) was 86wt.%. Further detailed characterization of CNTs is reported in supplementary information in section S1 and Figure S1a-e.

PPR/CNT nanocomposite FFF filaments were prepared by melt-blending using a co-rotating (Coperion ZSK 18, Germany) twin-screw extruder (see, Figure 1). This was equipped with screws of 18 mm diameter with a L/D ratio of 40. The temperatures in the 1st, 3rd, 5th, 7th and 9th zones of the extruder were 170, 190, 200, 210, and 220 °C, respectively while the die temperature was kept at 220 °C with a screw speed of 200 rpm. Before compounding, PPR and CNTs were vacuum dried at 100 ^{o}C and 0.4 bar for 6 h. For better mixing of CNTs in PPR matrix, both the materials were manually pre-mixed in the presence of acetone (solvent). Around 5-10 mL of acetone was used for each 1 kg batch of PPR/CNT. Due to the presence of the solvent, CNTs are coated onto the surface of micron-scale PPR granules [32]. The polymer composite filament was extruded using a circular die of 1.80 mm. To ensure uniformity of the target filament diameter (i.e., 1.75 mm), the extruder makes use of a puller mechanism. PPR/CNT composite filaments were prepared by mixing varying amounts of CNTs (0, 4, 6, 8 wt. % in the final filament) and are designated as PPR-0, PPR-4, PPR-6 and PPR-8.

CAD models were constructed in Solid Works to create 3D printable STL files of the specimens for FFF printing of PPR/CNT specimens using a Creator Pro 3D printer (Zhejiang Flashforge 3D technology Co., LTD). The filament was fed into a 0.4 mm diameter nozzle by a feeding pressure mechanism via a driver motor and a counter-rotating set of grooved gears. Process parameters such as nozzle tip temperature (230 ^{o}C), bed temperature (115 ^{o}C), layer height (0.2 mm), infill density

(100%) and extrusion width (0.4 mm) were kept the same for all the samples, i.e., process optimization for PPR/CNT blends is left for future work. For mechanical and piezoresistive analyses, the test specimens were printed in two print-directions i.e., 0^o and 90^o and they have been designated as 0^o/PPR-x or 90^o/PPR-x where "0" and "90" stand for printing direction and "x" indicates loading of CNTs in wt.%. For example, composites prepared by mixing 4 wt. % CNT and printed in 0^o or 90^o printing direction have been designated as 0^o/PPR-4 or 90^o/PPR-4, respectively. Furthermore, 2D auxetic structures of 30% relative density with re-entrant and S-unit cell geometry were printed using PPR-4.

The surface morphologies of as-received CNTs and cross-sectional fracture surfaces of PPR/CNT nanocomposites were analysed using Nova Nano SEM 50 series, operated at 10 kV to examine the microstructure and the dispersion state of CNTs in the PPR matrix. The samples for SEM were coated with a thin layer of Au (~10 nm) prior to examination by sputter coating. The DC electrical conductivity of the PPR/CNT nanocomposites samples was measured using the four-probe technique Van der Pauw method. For this purpose, 3D printed samples of size 10 x 10 x 2 mm^3 were created, which gives an average value of resistivity (does not assess possible non-isotropy in the 0^o vs. 90^o directions). To ensure conductive contact, silver paste was applied on the four corners of the sample which facilitates electrical contact between the electrodes and the sample. Piezoresistivity tests were conducted by measuring the change in electrical resistance using a Tektronix DMM 4050 multimeter on dogbone samples subjected to tensile loading. The tensile mechanical tests were performed in Zwick-Roell UTM and the grip-to-grip distance was set to 35 mm. Silver paste was applied on the contact surface to minimize contact resistance between the electrode and the sample. The piezoresistive response during uniaxial monotonic loading was evaluated at 5 mm/min crosshead speed. Likewise, the piezoresistive response during cyclic

loading was evaluated at maximum strain of 5% with a crosshead speed of 5 mm/min. Strain ratio (min strain/max strain) was set to 0.03 to avoid specimen buckling due to hysteresis. Furthermore, mechanical and piezoresistive response was evaluated under tensile cyclic loading with increasing strain amplitude (1% increase in peak strain after every cycle).

Results and Discussion

Both quasi-static and cyclic mechanical and sensing behaviour of the additively manufactured PPR/CNT composites under tensile loading is discussed, followed by quasi-static behaviour of their 2D lattices under tensile loading. Relevant PPR/CNT microstructural observations and trends, such as crystallinity, are discussed and related to the electrical, mechanical, and piezoresistive properties (see section S2).

Average DC electrical conductivity of PPR/CNT AM composites

Average DC electrical conductivity of FFF-printed PPR/CNT composite samples is shown in Figure 2, as a function of CNT content, based on the method described earlier. The conductivity of the composite increases monotonically with increasing CNT content and attains a sharp upswing (~six orders of magnitude) at ~2wt.% CNT loading, signifying the formation of electro-conductive paths within the PPR matrix, as expected. The electrical percolation threshold (the minimum filler loading where the first continuous conductive network forms within the insulating polymer matrix) of PPR/CNT composite is obtained by plotting the conductivity as a function of CNT content and performing data-fitting using the usual power law form:

$$\sigma = \sigma_0(\rho - \rho_c)^{\beta} \quad (1)$$

where σ is the electrical conductivity of the composite, σ_0 is intrinsic conductivity constant of the CNT, β is the critical exponent (the critical exponent which is related to the system dimensionality), ρ is the weight fraction of the CNT and ρ_c is the weight fraction of the CNT at

percolation threshold. It can be seen (inset Figure 2) that linear regression data-fitting gives the slope (i.e., critical exponent), $\beta = 2.72$ and percolation threshold, $\rho_c = 1.4$ wt.%. The occurrence of percolation threshold at low loadings is a direct consequence of effective processing, and here is affected not only by the feedstock fabrication, but also by the FFF printing comprising shear flow induced kneading and mixing.

Mechanical and piezoresistive response of PPR/CNT AM composites under quasi-static monotonic tensile loading

Figure 3 shows the representative stress-strain response, elastic modulus, and yield strength of the neat PPR and PPR/CNT nanocomposite samples for both the 0^o and 90^o specimen configurations. Elastic modulus is calculated over the initial linear region of the stress – strain response (up to a strain (ε) of 3.92%, 4.02%, 4.1% and 4.12% for 0^o/PPR-0, 0^o/PPR-4, 0^o/PPR-6 and 0^o/PPR-8 samples, and up to a strain (ε) of 3.14%, 3.23%, 3.24% and 3.27% for 90^o/PPR-0, 90^o/PPR-4, 90^o/PPR-6 and 90^o/PPR-8 samples, respectively). Yield stress of the samples was calculated using the offset method for a plastic strain of 0.1%. It can be observed from the plots that the mechanical properties of the FFF nanocomposites are a strong function of CNT loading and printing direction (0^o and 90^o) (see Table 1 and 2). The Tables and Figure 3 show that the elastic modulus and yield strength of the PPR/CNT composites increase with increasing CNT content. The 0^o samples (0^o/PPR-8), exhibit maximum elastic modulus and yield stress increase of 56% and 52%, respectively, while lower improvement is observed for 90^o samples (see Table 2). The enhancement of elastic modulus and yield stress indicate that the uniform dispersion of CNTs has resulted in effective load transfer from the PPR matrix to CNTs, enabling stiffer and stronger mechanical response of the nanocomposites [33]. Additionally, as is common for thermoplastics like PPR, the expected and noted increase in crystallinity due to the addition of CNTs into the PPR

matrix has also contributed towards reinforcement and stiffening of PPR/CNT composites as well, as shown via DSC and XRD (see Figure S4 and S5). The lower improvement in elastic modulus and yield stress observed for 90^o samples is attributed to the degree of adhesion between adjacent beads of the printed parts, as is common in FFF printing [34]. Note that the bead-bead interactions are dictated by the size and shape of geometry being printed and print-orientation, even for the same process parameters (see Figure S9). The reduction in failure strain and toughness of samples with increasing CNT content is noted and is usually attributed to the reduced mobility of the polymer chain that arises from the interaction of the PPR matrix with the CNTs, as well as the enhanced crystallinity. The addition of CNTs at all wt. % considered here imparts a useful piezoresistive sensing capability, unavailable in the baseline PPR structures. The piezoresistive response of PPR/CNT for 0° and 90° dogbone samples comprising different weight fractions of CNT under monotonic tensile load is displayed in Figure 4, to elucidate the effect of CNT loading and printing direction on piezoresistive behaviour of these AM nanocomposites. The sensitivity of PPR/CNT composites to strain is typically quantified via the gauge factor (k) given by:

$$k = \frac{1}{R_0}\frac{\Delta R}{\Delta \varepsilon} \tag{2}$$

where R_0 is the initial no-load ($\varepsilon = 0$) resistance of the nanocomposite, $\Delta R = (R - R_0)$ is the change in resistance, $R(\varepsilon)$ is the resistance at any strain ε imposed on the composite sample and $\Delta\varepsilon$ is the change in imposed strain. During mechanical loading, as the applied strain increases, the average distance between conducting paths (CNTs) increases, causing a change in resistance of the polymer nanocomposites [35]. Further increases in strain increases the separation distance between the adjacent CNTs; the electrical conductivity change (or conversely change in resistance) of the nanocomposite is attributed to electron tunnelling and hopping mechanisms at the CNT-CNT junctions.

The gauge factor evaluated in the elastic regime indicates the strain sensitivity, while the gauge factor evaluated in the inelastic regime indicates the damage sensitivity. The PPR/CNT 0° dogbone specimens comprising 4, 6 and 8 wt.% CNT loading exhibit piezoresistive strain sensitivity gage factor k_s of 17.4 ($\varepsilon \leq 8.52\%$), 14.7 ($\varepsilon \leq 8.62\%$) and 10.1 ($\varepsilon \leq 8.79\%$), respectively before yield (see Table 3). The piezoresistive response of 0°/PPR-4 composite in the inelastic regime was approximated by a bi-linear fit with regime I over $8.52\% < \varepsilon \leq 51\%$, giving damage sensitivity $k_d^I = 78.8$ and regime II over $51\% < \varepsilon \leq 104\%$, giving $k_d^{II} = 411.3$. Similarly, the damage sensitivity in inelastic regime I, $k_d^I = 33$ ($8.62\% < \varepsilon \leq 30\%$) and in inelastic regime II, $k_d^{II} = 54.29$ ($30\% < \varepsilon \leq 46.5\%$) was obtained for 0°/PPR-6 composites. The 0°/PPR-8 composites exhibit, $k_d^I = 17.8$ ($3.2\% < \varepsilon \leq 15\%$) and $k_d^{II} = 26.1$ ($15\% < \varepsilon \leq 33.2\%$) as summarized in Table 3. The gauge factors in regimes I and II are higher compared to those in the elastic regime as the resistance evolution in regimes I and II (hysteretic regime) is dominated by inelastic processes such as damage and plasticity. Similarly, the 90° dogbone samples with 4, 6 and 8 wt. % of CNT loading show piezoresistive strain sensitivity k_s of 4.5 ($\varepsilon \leq 7.42\%$), 3.6 ($\varepsilon \leq 7.39\%$) and 2.9 ($\varepsilon \leq 7.55\%$) respectively before yield (see Table 4). In case of 90° composites, the piezoresistive response in the inelastic regime was approximated by linear fit with regime I over $7.42\% < \varepsilon \leq 30\%$ for 90°/PPR-4, $7.39\% < \varepsilon \leq 25\%$ for 90°/PPR-6 and $7.55\% < \varepsilon \leq 21.6\%$ for 90°/PPR-8 samples, giving damage sensitivity, k_d^I of 15.5, 9.7 and 5.9 respectively (see Table 4). At lower CNT loading, both 0° and 90° samples show higher gauge factors within the elastic regime. This is due to a smaller number of conductive paths within the PPR matrix and therefore, change in resistance is relatively large to small, applied strain. CNTs form a denser network at high loading of CNT (i.e., 6 and 8 wt. %) in the matrix and the change in resistance is naturally reduced, leading to lower gauge factor with increase in CNT content. Thus, one might consider an

optimum CNT loading that is a compromise between sensing and mechanical reinforcement, suggesting tunability as studied here.

The piezoresistive sensitivity and the mechanical response of PPR/CNT composites printed in 0° direction were found to be higher than those for 90^{o} samples, confirming the influence of printing-induced mechanical and multifunctional anisotropy of FFF AM composites. 0°/PPR samples (Figure 4a) displays higher piezoresistive sensitivity (gauge factor, k) and mechanical properties (Table 1 and 2) as the applied load is resisted by the fibre-like printed beads whose longitudinal direction is parallel to the loading direction. In such loading scenario, each adjacent extruded bead is loaded along its longitudinal direction, contributing to enhanced mechanical performance, while in the 90° samples the loading direction is perpendicular to the printing direction and load is transferred through the relatively compliant and weak inter-bead weak interfaces. SEM micrographs (Figure S6a) of hand-fractured surfaces (at room temperature) of 0^{o}/PPR-4 samples clearly reveals coarser fibrillated structures than in the 90^{o} cases and displays the presence of fibril type continuous networks with the appearance of crazing. Thus, the fracture surface morphology undergoes a transition from extensive fibrillated networks to crazing-mediated restriction of plastic flow across the composition regime of 0° samples, while 90^{o} samples display continuous brittle fracture like morphology (Figure S6b). A second reinforcement that is hypothesized, but was not studied, is that the filament fabrication and FFF printing process both act to align the CNTs along the printed fibre direction, thus providing an aligned-CNT nanocomposite morphology where anisotropy in stiffness has been observed in past work with non-AM aligned-CNT polymer matrix nanocomposites [36].

Mechanical and piezoresistive response of PPR/CNT AM composites under cyclic loading

The performance of PPR/CNT nanocomposites were also assessed under strain-controlled tensile cyclic loading (at 5 mm/min, same as in the monotonic testing to failure in the last section) up to 100 loading-unloading cycles with constant strain amplitude, and also repetitive tensile cyclic loading with increasing strain amplitude up to 10 cycles. Samples comprising 4 wt.% CNT loading were chosen for cyclic tests as this formulation exhibited good piezoresistive response as well as the best balance of mechanical properties including strain tolerance (100%) and high toughness under monotonic tensile loading (see Figure 4, and Table 1), as discussed in previous section. Repetitive tensile cyclic loading-unloading tests with constant and increasing strain amplitude help to assess the durability, long-term performance, and the hysteresis response of the nanocomposites. The stress increases in response to applied strain up to a maximum and returns to zero upon unloading forming the hysteresis loop (see Figures 5a-b and S7). Strain-controlled constant amplitude cyclic tests indicate that secant elastic modulus increases with number of cycles in the neat PPR and decreases in PPR/CNT AM nanocomposites, while the maximum strain imposed is less than yield strain, and from a higher starting point than the 0 wt.% case. Interestingly, the maximum stress decays with cycling as observed from the stress-strain curves of 1^{st}, 50^{th} and 100^{th} cycles (Figure 5 and 6). This is likely due to polymer chain relaxation phenomenon [37]. Figures 5, 6 and S7 also show that the maximum and minimum electrical resistances reduce slowly as the number of cycles increase. This is attributed to CNT-polymer chains interactions (supported by SEM and Raman spectroscopy; Figure S2 and S3) where during loading, the PPR chains are strained into in entropically unstable condition following the mechanical deformation direction resulting in CNT rotation towards the stretching direction. The average distance between individual CNTs increases leading to larger higher change in electrical resistance. As the cycling

continues, the PPR chains gradually return to their more entropically stable condition. Subsequently, the average CNT distance reduces and the sample gains back some of its electrical conductivity due to these hysteretic effects. Although the reduction in stress is small (~17%) between the 1st and 50th cycle, the stress during 50th and 100th cycle is almost the same (a difference of ~2.1%), showing that the mechanical performance of the nanocomposites is relatively stable [38] up to 100 repetitive stretch/release cycles for an imposed strain of 5%. The instantaneous gauge factor during the 50th and 100th loading part of cyclic tests (See Figure 7b) relative to the first cycle indicates stable piezoresistive performance under constant amplitude cyclic loading. The difference in peak resistance between 50th and 100th cycle is ~1.5%. Dissipated energy as a function of cycles (Figures 5 and 6) confirms the change in stress peaks with loading and unloading cycles. The dissipated energy decreases as the number of cycles increases primarily due to the viscoelastic nature of PPR. The decrease in dissipated energy between 50th and 100th cycle is ~6.2%. The mechanical and piezoresistive performance of PPR/CNT samples under increasing cyclic loading up to 10 repetitive cycles is shown in Figure S8. The piezoresistive response shown in Figures 5, 6, S7 and S8, shows single peak pattern indicating a proper relation between electrical resistance and strain for sensing applications [39]. Further, the printing direction also affects the sensitivity, long term performance, durability, and hysterics response of polymer composites. It is clear from the Figures 5, 6, S7 and S8 that the samples printed in 0° direction (0°/PPR-4) show higher values in terms of change in resistance and stress than 90° (90°/PPR-4) samples. During cyclic loading-unloading tests 0°/PPR-4 sample showed almost double sensitivity (gage factor) compared to 90°/PPR-4 sample, showing non-isotropy in sensing ability with greater anisotropy ratio than the mechanical properties.

As a demonstration of the use of the AM nanocomposites, 2D lattice structures possessing a relative density of 30% were additively manufactured using the 4 wt.% PPR/CNT nano-engineered filament (Figure 7). The re-entrant and S-unit cell geometries impart negative Poisson's ratio, usually referred to as auxetic behaviour [40], to the lattice structure, which can be useful in applications such as knee and elbow pads and stents[41]. These auxetic lattice structures were tested under uniaxial tension and the load-displacement behaviour together with their piezoresistive sensing response, as shown in Figure 7 (see video V1 in SI, Section S3 for stress and sensing time-synchronized deformation of the loaded auxetic lattice structure). The mechanical properties of these 2D auxetic lattice structures exhibit the usual scaling with relative density as expected, although neat (PPR-0) re-entrant structure exhibits higher modulus (+3840%) and strength (+25%) as well as lower strain tolerance (-96%), compared to the S-unit cell structure of the same relative density. However, both re-entrant and S-shaped CNT-engineered auxetic structures (PPR/CNT-4) exhibit improved modulus (+51.5% and +15.4%) and strength (+73.1% and +63.3%) with concomitant reduction in failure strain (-37.9% and -50.8%) respectively, compared to their non-reinforced counterparts (PPR-0) as quantified in Table 5. Note that the S-unit cell geometry significantly reduces stress concentration effects [42] and promotes strain tolerance compared to the re-entrant structure of the same relative density, facilitating the design of auxetics with tuneable strain tolerance. Interestingly, comparison of the piezoresistive response of the auxetic structures with PPR/CNT 4 wt.% shows a considerable change in strain- and damage-sensitivity for the auxetic lattice structures compared to bulk counterparts. The strain sensitivity, k_s of PPR-4 re-entrant and S-unit cell auxetic lattice structures (of 30% relative density) is found to be 13.2 and 0.06 over $0 \leq \varepsilon \leq 4.45\%$ and $0 \leq \varepsilon \leq 4.73\%$ (see Table 6) respectively. On the other hand, the damage sensitivity, k_d of PPR-4 re-entrant and S-unit cell structures in the inelastic regime was

found to be 53.7 and 1.23 over $4.45\% \leq \varepsilon \leq 14.1\%$ and $4.73 \leq \varepsilon \leq 196\%$ respectively, offering insight into to rate of damage evolution. Higher damage sensitivity indicates faster damage progression and fracture of ligaments within the lattice structure under tension due to stress concentrations. The results obtained from 2D auxetic structures demonstrate that the mechanical and piezoresistive characteristics of PPR/CNT auxetic lattice structures can be tailored by tuning the cell-topology and relative density besides the CNT content in the PPR matrix.

Conclusions

This study presents tuneable mechanical and piezoresistive characteristics of bulk and PPR/CNT auxetic structures processed via FFF AM. The mechanical and piezoresistive response of the bulk and PPR/CNT auxetic structures, both under monotonic tensile and repetitive cyclic tensile loading, were studied considering the two principal printing directions (0^o & 90^o) towards self-sensing biomedical applications. CNTs in the PPR nanocomposite filament feedstock are shown to reinforce the neat polymer, including contributions from enhanced crystallinity in the PPR. The printing directions significantly affect the performance of the AM-enabled nanocomposites: the samples printed in 0^o direction show a maximum elastic modulus and yield stress improvement of 56% and 52%, respectively, while lower improvement was observed in case of 90^o samples (maximum elastic modulus and yield stress improvement of 34% and 12%, respectively). These FFF-printed bulk nanocomposites also display electrical percolation (1.48 wt.%) which indicates good dispersion of CNTs within the polymer matrix. Furthermore, the piezoresistive response confirms that the samples printed in 0^o direction exhibit more pronounced piezoresistive response over a large strain range with high values of gauge factor (strain sensitivity, $k_s = 10.1 - 17.4$ before yield, damage sensitivity, $k_d^I = 19.8 - 78.8$ and $k_d^{II} = 26.1 - 411.3$ in the hysteretic regime I and II) than the samples printed in the 90^o direction (strain sensitivity, $k_s = 2.9 - 4.5$ in

elastic regime, damage sensitivity, $k_d^I = 5.9 - 15.5$ in the inelastic regime). These results suggest that both the mechanical and piezoresistive properties of the AM-enabled nanocomposites heavily depend on the degree of adhesion between adjacent beads, similar to many FFF AM materials, besides other factors. The piezoresistive response of nanocomposites under tensile cyclic loading with constant strain amplitude (within the elastic regime) and with increasing strain amplitude showed consistent piezoresistive behaviour as the electrical resistance change of PPR/CNT followed the mechanical deformation, both during loading and unloading with a slight discrepancy primarily attributed to the viscoelastic nature of the PPR/CNT composite. The extent of such a difference correlates with the amount of accumulated damage. Likewise, the AM-enabled nanocomposites remained conductive and show good piezoresistivity even after 100 repetitive loading-unloading cycles under a strain amplitude of 5%.

CNT-engineered re-entrant and S-unit cell auxetic structures (30% relative density) were created with the 4 wt.% PPR/CNT FFF filaments and shown to exhibit improved modulus (+51.5% and +15.4%) and strength (+73.1% and +63.3%) respectively, relative to their unreinforced PPR counterparts. Although the S-unit cell geometry is not efficient in terms of strength and stiffness, its structure significantly reduces stress concentration and promotes strain tolerance. The strain and damage sensitivity of the re-entrant lattice is found to be much higher than that of S-unit cell lattices. Higher damage sensitivity of re-entrant structure indicates faster destruction of the electrically conductive network and fracture of ligaments within the lattice structure under tension. These FFF-printable AM nanocomposites with good electrical and mechanical properties along with tuneable piezoresistive response are a likely candidate for making highly strain- and/or damage-sensitive structures. The results suggest that these multifunctional materials can self-sense strain as well as instantaneous and accumulated damage. The demonstrated PPR/CNT auxetic

structures underscore the potential of AM-enabled PPR/CNT composites for the creation of smart patient-specific biomedical devices. For example, self-sensing orthopaedic bracing used for the treatment of complex three-dimensional deformity in adolescent scoliosis patients would offer the ability to sense and accurately adjust the stiffness of the bracing in different directions, and to determine the optimal timing and manner of brace adjustments. These requirements remain unmet with conventional rigid bracing made from passive materials via conventional manufacturing approaches. Deployment of this technology poses several challenges in realizing any medical application, such as scoliosis bracing with spatially and directionally tuneable cellular architecture (so as to tailor the strength and stiffness) and locally tuneable shape transformation upon demand. The challenges associated with the design, fabrication, and then human-trial will be addressed in a subsequent study. Such biomedical braces have tremendous implications for over 68,000 children being treated each year in the U.S. alone for idiopathic scoliosis, as well as patients suffering from many other orthopaedic conditions.

Supporting Information

Supporting information includes characterization of MWCNTs and additively manufactured PPR/MWCNT composites via SEM, TEM, XRD, Raman, TGA and DSC techniques and video showing stress and sensing time-synchronized deformation of the loaded auxetic lattice structure.

Acknowledgements
Authors gratefully acknowledge financial support from the ADNOC under Award No: EX2016-000010. Authors would like to acknowledge the support of Johannes Schneider.

Author contributions
S. Kumar conceived the idea. Pawan Verma and J. Ubaid fabricated samples via 3D printing and conducted experiments. S. Kumar and B.L. Wardle guided the project. All authors discussed the results and contributed to manuscript preparation.

References
(1) Kong, Y. L.; Tamargo, I. A.; Kim, H.; Johnson, B. N.; Gupta, M. K.; Koh, T.-W.; Chin, H.-A.; Steingart, D. A.; Rand, B. P.; McAlpine, M. C. 3D Printed Quantum Dot Light-Emitting Diodes. *Nano Letters* **2014**, *14* (12), 7017-7023, doi: 10.1021/nl5033292. DOI: 10.1021/nl5033292. Bartlett, N. W.; Tolley, M. T.; Overvelde, J. T. B.; Weaver, J. C.; Mosadegh, B.; Bertoldi, K.;

Whitesides, G. M.; Wood, R. J. A 3D-printed, functionally graded soft robot powered by combustion. *Science* **2015**, *349* (6244), 161, 10.1126/science.aab0129.
(2) Arif, M.; Alhashmi, H.; Varadarajan, K.; Koo, J. H.; Hart, A.; Kumar, S. Multifunctional performance of carbon nanotubes and graphene nanoplatelets reinforced PEEK composites enabled via FFF additive manufacturing. *Composites Part B: Engineering* **2020**, *184*, 107625.
(3) Lee, J.-Y.; An, J.; Chua, C. K. Fundamentals and applications of 3D printing for novel materials. *Applied Materials Today* **2017**, *7*, 120-133. DOI: https://doi.org/10.1016/j.apmt.2017.02.004. Rajkumar, A. R.; Shanmugam, K. Additive manufacturing-enabled shape transformations via FFF 4D printing. *Journal of Materials Research* **2018**, *33* (24), 4362-4376. DOI: 10.1557/jmr.2018.397 From Cambridge University Press Cambridge Core.
(4) Nadgorny, M.; Ameli, A. Functional polymers and nanocomposites for 3D printing of smart structures and devices. *ACS applied materials & interfaces* **2018**, *10* (21), 17489-17507.
(5) Park, S.; Shou, W.; Makatura, L.; Matusik, W.; Fu, K. 3D printing of polymer composites: Materials, processes, and applications. *Matter* **2022**, *5* (1), 43-76. DOI: https://doi.org/10.1016/j.matt.2021.10.018.
(6) Kumar, S.; Wardle, B. L.; Arif, M. F.; Ubaid, J. Stress Reduction of 3D Printed Compliance-Tailored Multilayers. *Prof. Wardle via Barbara Williams* **2017**. (acccessed 2022/01/18/12:42:38). From dspace.mit.edu.
(7) Hofmann, M. 3D Printing Gets a Boost and Opportunities with Polymer Materials. *ACS Macro Letters* **2014**, *3* (4), 382-386, doi: 10.1021/mz4006556. DOI: 10.1021/mz4006556. Singh, M.; Haverinen, H. M.; Dhagat, P.; Jabbour, G. E. Inkjet printing—process and its applications. *Advanced materials* **2010**, *22* (6), 673-685. Tian, X.; Liu, T.; Yang, C.; Wang, Q.; Li, D. Interface and performance of 3D printed continuous carbon fiber reinforced PLA composites. *Composites Part A: Applied Science and Manufacturing* **2016**, *88*, 198-205. DOI: https://doi.org/10.1016/j.compositesa.2016.05.032. Guo, S.-z.; Yang, X.; Heuzey, M.-C.; Therriault, D. 3D printing of a multifunctional nanocomposite helical liquid sensor. *Nanoscale* **2015**, *7* (15), 6451-6456, 10.1039/C5NR00278H. DOI: 10.1039/c5nr00278h. Wei, X.; Li, D.; Jiang, W.; Gu, Z.; Wang, X.; Zhang, Z.; Sun, Z. 3D printable graphene composite. *Scientific reports* **2015**, *5*, 11181.
(8) Gupta, T. K.; Choosri, M.; Varadarajan, K.; Kumar, S. Self-sensing and mechanical performance of CNT/GNP/UHMWPE biocompatible nanocomposites. *Journal of Materials Science* **2018**, *53* (11), 7939-7952. Mora, A.; Verma, P.; Kumar, S. Electrical conductivity of CNT/polymer composites: 3D printing, measurements and modeling. *Composites Part B: Engineering* **2020**, *183*, 107600.
(9) Kumar, S.; Gupta, T. K.; Varadarajan, K. Strong, stretchable and ultrasensitive MWCNT/TPU nanocomposites for piezoresistive strain sensing. *Composites Part B: Engineering* **2019**, *177*, 107285.
(10) Rett, J. P.; Traore, Y. L.; Ho, E. A. Sustainable Materials for Fused Deposition Modeling 3D Printing Applications. *Advanced Engineering Materials* **2021**, *23* (7), 2001472, https://doi.org/10.1002/adem.202001472. DOI: https://doi.org/10.1002/adem.202001472 (acccessed 2022/01/14).
(11) Wu, A. S.; Chou, T.-W. Carbon nanotube fibers for advanced composites. *Materials Today* **2012**, *15* (7), 302-310. DOI: https://doi.org/10.1016/S1369-7021(12)70135-9. Gibson, R. F. A review of recent research on mechanics of multifunctional composite materials and structures. *Composite structures* **2010**, *92* (12), 2793-2810. Wang, B.; Li, Z.; Wang, C.; Signetti, S.; Cunning,

B. V.; Wu, X.; Huang, Y.; Jiang, Y.; Shi, H.; Ryu, S.; Pugno, N. M.; Ruoff, R. S. Folding Large Graphene-on-Polymer Films Yields Laminated Composites with Enhanced Mechanical Performance. *Advanced Materials* **2018**, *30* (35), 1707449. DOI: https://doi.org/10.1002/adma.201707449. Bae, J.-S.; Lee, Y.-S.; Li, J.; Liang, J.; Chen, D.; Pei, Q.; Lee, S.-B. The Feasibility of Healable Electronics and Mechanical Behavior of Silver Nanowire (AgNW)/Healable Polymer Composite. *Advanced Materials Technologies* **2018**, *3* (6), 1700364. DOI: https://doi.org/10.1002/admt.201700364. Ji, D.; Choi, S.; Kim, J. A Hydrogel-Film Casting to Fabricate Platelet-Reinforced Polymer Composite Films Exhibiting Superior Mechanical Properties. *Small* **2018**, *14* (26), 1801042. DOI: https://doi.org/10.1002/smll.201801042. Gungor, A. The physical and mechanical properties of polymer composites filled with Fe-powder. *Journal of Applied Polymer Science* **2006**, *99* (5), 2438-2442. DOI: https://doi.org/10.1002/app.22637. Balasubramaniam, B.; Sathiyan, G.; Palani, G. S.; Iyer, N. R.; Gupta, R. K. Fiber Reinforced Polymer Nanocomposites for Structural Engineering Applications. In *Materials Science and Technology*, pp 1-20. Lu, H. H.; El-Amin, S. F.; Scott, K. D.; Laurencin, C. T. Three-dimensional, bioactive, biodegradable, polymer–bioactive glass composite scaffolds with improved mechanical properties support collagen synthesis and mineralization of human osteoblast-like cells in vitro. *Journal of Biomedical Materials Research Part A* **2003**, *64A* (3), 465-474. DOI: https://doi.org/10.1002/jbm.a.10399.

(12) Thostenson, E. T.; Ren, Z.; Chou, T.-W. Advances in the science and technology of carbon nanotubes and their composites: a review. *Composites Science and Technology* **2001**, *61* (13), 1899-1912. DOI: https://doi.org/10.1016/S0266-3538(01)00094-X.

(13) Bekas, D. G.; Hou, Y.; Liu, Y.; Panesar, A. 3D printing to enable multifunctionality in polymer-based composites: A review. *Composites Part B: Engineering* **2019**, *179*, 107540. DOI: https://doi.org/10.1016/j.compositesb.2019.107540. Reddy, S. K.; Kumar, S.; Varadarajan, K. M.; Marpu, P. R.; Gupta, T. K.; Choosri, M. Strain and damage-sensing performance of biocompatible smart CNT/UHMWPE nanocomposites. *Materials Science and Engineering: C* **2018**, *92*, 957-968. DOI: https://doi.org/10.1016/j.msec.2018.07.029.

(14) Chung, D. D. L. A review of multifunctional polymer-matrix structural composites. *Composites Part B: Engineering* **2019**, *160*, 644-660. DOI: https://doi.org/10.1016/j.compositesb.2018.12.117.

(15) Song, Q.; Ye, F.; Yin, X.; Li, W.; Li, H.; Liu, Y.; Li, K.; Xie, K.; Li, X.; Fu, Q.; Cheng, L.; Zhang, L.; Wei, B. Carbon Nanotube–Multilayered Graphene Edge Plane Core–Shell Hybrid Foams for Ultrahigh-Performance Electromagnetic-Interference Shielding. *Advanced Materials* **2017**, *29* (31), 1701583. DOI: https://doi.org/10.1002/adma.201701583. Wen, L.; Li, F.; Cheng, H.-M. Carbon Nanotubes and Graphene for Flexible Electrochemical Energy Storage: from Materials to Devices. *Advanced Materials* **2016**, *28* (22), 4306-4337. DOI: https://doi.org/10.1002/adma.201504225. Yin, Z.; Cui, C.; Chen, H.; Duoni; Yu, X.; Qian, W. The Application of Carbon Nanotube/Graphene-Based Nanomaterials in Wastewater Treatment. *Small* **2020**, *16* (15), 1902301. DOI: https://doi.org/10.1002/smll.201902301. Lv, T.; Liu, M.; Zhu, D.; Gan, L.; Chen, T. Nanocarbon-Based Materials for Flexible All-Solid-State Supercapacitors. *Advanced Materials* **2018**, *30* (17), 1705489. DOI: https://doi.org/10.1002/adma.201705489. Hwang, I.; Kim, H. N.; Seong, M.; Lee, S.-H.; Kang, M.; Yi, H.; Bae, W. G.; Kwak, M. K.; Jeong, H. E. Multifunctional Smart Skin Adhesive Patches for Advanced Health Care. *Advanced Healthcare Materials* **2018**, *7* (15), 1800275. DOI: https://doi.org/10.1002/adhm.201800275. Rathore, D. K.; Prusty, R. K.; Ray, B. C. Mechanical, thermomechanical, and creep performance of CNT embedded epoxy at elevated temperatures: An emphasis on the role of carboxyl

functionalization. *Journal of Applied Polymer Science* **2017**, *134* (21). DOI: https://doi.org/10.1002/app.44851. Tesh, S. J.; Scott, T. B. Nano-Composites for Water Remediation: A Review. *Advanced Materials* **2014**, *26* (35), 6056-6068. DOI: https://doi.org/10.1002/adma.201401376. Lee, J.-J.; Park, E.-W.; Hyun, S.-H. Performance and Evaluation of Cu-based Nano-composite Anodes for Direct Utilisation of Hydrocarbon Fuels in SOFCs. *Fuel Cells* **2010**, *10* (1), 145-155. DOI: https://doi.org/10.1002/fuce.200800186. Jiang, Y.; Cheng, M.; Shahbazian-Yassar, R.; Pan, Y. Direct Ink Writing of Wearable Thermoresponsive Supercapacitors with rGO/CNT Composite Electrodes. *Advanced Materials Technologies* **2019**, *4* (12), 1900691. DOI: https://doi.org/10.1002/admt.201900691. Benson, J.; Kovalenko, I.; Boukhalfa, S.; Lashmore, D.; Sanghadasa, M.; Yushin, G. Multifunctional CNT-Polymer Composites for Ultra-Tough Structural Supercapacitors and Desalination Devices. *Advanced Materials* **2013**, *25* (45), 6625-6632. DOI: https://doi.org/10.1002/adma.201301317. Shieh, Y.-T.; Liu, G.-L.; Twu, Y.-K.; Wang, T.-L.; Yang, C.-H. Effects of carbon nanotubes on dynamic mechanical property, thermal property, and crystal structure of poly(L-lactic acid). *Journal of Polymer Science Part B: Polymer Physics* **2010**, *48* (2), 145-152. DOI: https://doi.org/10.1002/polb.21872. Andrew, J. J.; Verma, P.; Kumar, S. Impact behavior of nanoengineered, 3D printed plate-lattices. *Materials & Design* **2021**, *202*, 109516. DOI: https://doi.org/10.1016/j.matdes.2021.109516.

(16) Zhang, W.; Dehghani-Sanij, A. A.; Blackburn, R. S. Carbon based conductive polymer composites. *Journal of materials science* **2007**, *42* (10), 3408-3418. Cheeseman, B.; Safari, A.; Danforth, S.; Chou, T.-W. Carbon Nanotube Based Polymeric Composites—A Review. *Design, Manufacturing & Application of Composites* **2020**, 48-48.

(17) Verma, P.; Saini, P.; Malik, R. S.; Choudhary, V. Excellent electromagnetic interference shielding and mechanical properties of high loading carbon-nanotubes/polymer composites designed using melt recirculation equipped twin-screw extruder. *Carbon* **2015**, *89*, 308-317.

(18) Bauhofer, W.; Kovacs, J. Z. A review and analysis of electrical percolation in carbon nanotube polymer composites. *Composites Science and Technology* **2009**, *69* (10), 1486-1498. DOI: https://doi.org/10.1016/j.compscitech.2008.06.018.

(19) Zeng, X.; Xu, X.; Shenai, P. M.; Kovalev, E.; Baudot, C.; Mathews, N.; Zhao, Y. Characteristics of the Electrical Percolation in Carbon Nanotubes/Polymer Nanocomposites. *The Journal of Physical Chemistry C* **2011**, *115* (44), 21685-21690. DOI: 10.1021/jp207388n.

(20) Kinloch, I. A.; Suhr, J.; Lou, J.; Young, R. J.; Ajayan, P. M. Composites with carbon nanotubes and graphene: An outlook. *Science* **2018**, *362* (6414), 547-553. DOI: 10.1126/science.aat7439 From NLM.

(21) Avilés, F.; Oliva-Avilés, A. I.; Cen-Puc, M. Piezoresistivity, Strain, and Damage Self-Sensing of Polymer Composites Filled with Carbon Nanostructures. *Advanced Engineering Materials* **2018**, *20* (7), 1701159. DOI: https://doi.org/10.1002/adem.201701159.

(22) Chen, X.; Zhang, X.; Xiang, D.; Wu, Y.; Zhao, C.; Li, H.; Li, Z.; Wang, P.; Li, Y. 3D printed high-performance spider web-like flexible strain sensors with directional strain recognition based on conductive polymer composites. *Materials Letters* **2022**, *306*, 130935. DOI: https://doi.org/10.1016/j.matlet.2021.130935.

(23) *Strain gauge data sheets*. HBK UK, 2021. https://www.hbm.com/en/2122/strain-gauge-datasheets/ (accessed 2021 01/10/2021). *Technical Databooks for Strain Gages and Accessories*. Vishay Precision Group, 2021. https://micro-measurements.com/knowledge-base/databooks (accessed 2021.

(24) Zetina-Hernández, O.; Duarte-Aranda, S.; May-Pat, A.; Canché-Escamilla, G.; Uribe-Calderon, J.; Gonzalez-Chi, P.; Avilés, F. Coupled electro-mechanical properties of multiwall carbon nanotube/polypropylene composites for strain sensing applications. *Journal of materials science* **2013**, *48* (21), 7587-7593. Zhao, J.; Dai, K.; Liu, C.; Zheng, G.; Wang, B.; Liu, C.; Chen, J.; Shen, C. A comparison between strain sensing behaviors of carbon black/polypropylene and carbon nanotubes/polypropylene electrically conductive composites. *Composites Part A: Applied Science and Manufacturing* **2013**, *48*, 129-136. DOI: https://doi.org/10.1016/j.compositesa.2013.01.004.
(25) Ha, M.; Lee, S.; Ko, H. Wearable and flexible sensors for user-interactive health-monitoring devices. *Journal of Materials Chemistry B* **2018**.
(26) Schlenzka, D.; Yrjönen, T. Bracing in adolescent idiopathic scoliosis. *J Child Orthop* **2013**, *7* (1), 51-55. DOI: 10.1007/s11832-012-0464-5 PubMed.
(27) Konieczny, M. R.; Senyurt, H.; Krauspe, R. Epidemiology of adolescent idiopathic scoliosis. *J Child Orthop* **2013**, *7* (1), 3-9. DOI: 10.1007/s11832-012-0457-4 PubMed.
(28) Akhoundi, B.; Nabipour, M.; Hajami, F.; Shakoori, D. An Experimental Study of Nozzle Temperature and Heat Treatment (Annealing) Effects on Mechanical Properties of High-Temperature Polylactic Acid in Fused Deposition Modeling. *Polymer Engineering & Science* **2020**, *60* (5), 979-987. DOI: https://doi.org/10.1002/pen.25353.
(29) *Standard Test Method for Melt Flow Rates of Thermoplastics by Extrusion Plastometer*.
(30) Arif, M. F.; Kumar, S.; Gupta, T. K.; Varadarajan, K. M. Strong linear-piezoresistive-response of carbon nanostructures reinforced hyperelastic polymer nanocomposites. *Composites Part A: Applied Science and Manufacturing* **2018**, *113*, 141-149.
(31) Shah, T. K.; Malecki, H. C.; Basantkumar, R. R.; Liu, H.; Fleischer, C. A.; Sedlak, J. J.; Patel, J. M.; Burgess, W. P.; Goldfinger, J. M. Carbon nanostructures and methods of making the same. Google Patents: 2014.
(32) Verma, P.; Kumar, A.; Chauhan, S. S.; Verma, M.; Malik, R. S.; Choudhary, V. Industrially viable technique for the preparation of HDPE/fly ash composites at high loading: Thermal, mechanical, and rheological interpretations. *Journal of Applied Polymer Science* **2018**, *135* (11), 459951.
(33) Cheng, Q.; Bao, J.; Park, J.; Liang, Z.; Zhang, C.; Wang, B. High mechanical performance composite conductor: Multi-walled carbon nanotube sheet/bismaleimide nanocomposites. *Advanced Functional Materials* **2009**, *19*, 3219-3225. DOI: 10.1002/adfm.200900663. Koziol, K.; Vilatela, J.; Moisala, A.; Motta, M.; Cunniff, P.; Sennett, M.; Windle, A. High-performance carbon nanotube fiber. *Science* **2007**, *318* (5858), 1892-1895.
(34) Arif, M.; Kumar, S.; Varadarajan, K.; Cantwell, W. Performance of biocompatible PEEK processed by fused deposition additive manufacturing. *Materials & Design* **2018**, *146*, 249-259.
(35) Cho, D.; Park, J.; Kim, J.; Kim, T.; Kim, J.; Park, I.; Jeon, S. Three-Dimensional Continuous Conductive Nanostructure for Highly Sensitive and Stretchable Strain Sensor. *ACS Applied Materials & Interfaces* **2017**, *9* (20), 17369-17378.
(36) Handlin, D.; Stein, I. Y.; Guzman de Villoria, R.; Cebeci, H.; Parsons, E. M.; Socrate, S.; Scotti, S.; Wardle, B. L. Three-dimensional elastic constitutive relations of aligned carbon nanotube architectures. *Journal of Applied Physics* **2013**, *114* (22), 224310. Gair Jr, J. L.; Lambeth, R. H.; Cole, D. P.; Lidston, D. L.; Stein, I. Y.; Kalfon-Cohen, E.; Hsieh, A. J.; Bruck, H. A.; Bundy, M. L.; Wardle, B. L. Strong process-structure interaction in stoveable poly (urethane-urea) aligned carbon nanotube nanocomposites. *Composites Science and Technology* **2018**, *166*, 115-124.

(37) Arzhakov, M. *Relaxation in Physical and Mechanical Behavior of Polymers*; CRC Press, 2019.
(38) Zhao, Z.; Shen, S.; Li, Y.; Zhang, X.; Su, J.; Li, H.; Ai, T.; Tang, D. Strain-sensing behavior of flexible polypropylene/poly(ethylene-co-octene)/multiwalled carbon nanotube nanocomposites under cyclic tensile deformation. *Polymer Composites* **2022**, *43* (1), 7-20, https://doi.org/10.1002/pc.26353. DOI: https://doi.org/10.1002/pc.26353 (acccessed 2022/01/14).
(39) Liu, H.; Gao, J.; Huang, W.; Dai, K.; Zheng, G.; Liu, C.; Shen, C.; Yan, X.; Guo, J.; Guo, Z. Electrically conductive strain sensing polyurethane nanocomposites with synergistic carbon nanotubes and graphene bifillers. *Nanoscale* **2016**, *8* (26), 12977-12989.
(40) Bertoldi, K.; Reis, P. M.; Willshaw, S.; Mullin, T. Negative Poisson's ratio behavior induced by an elastic instability. *Advanced materials* **2010**, *22* (3), 361-366.
(41) Li, X.; Wang, Q.; Yang, Z.; Lu, Z. Novel auxetic structures with enhanced mechanical properties. *Extreme Mechanics Letters* **2019**, *27*, 59-65.
(42) Meena, K.; Singamneni, S. A new auxetic structure with significantly reduced stress concentration effects. *Materials & Design* **2019**, *173*, 107779.
(43) Weiss, H.-R.; Tournavitis, N.; Nan, X.; Borysov, M.; Paul, L. Workflow of CAD/CAM scoliosis brace adjustment in preparation using 3D printing. *The open medical informatics journal* **2017**, *11*, 44.

ToC

Mechanical and piezoresistive performance of carbon nanotube doped thermoplastic nanocomposites enabled via FFF additive manufacturing is demonstrated. Further, the 2D multifunctional auxetics have significantly enhanced mechanical performance and exhibit tuneable strain- and damage-sensitivity, with application to self-sensing patient-specific biomedical devices, where the ability to sense strain can provide direct information for optimization of device design/fit over the course of treatment.

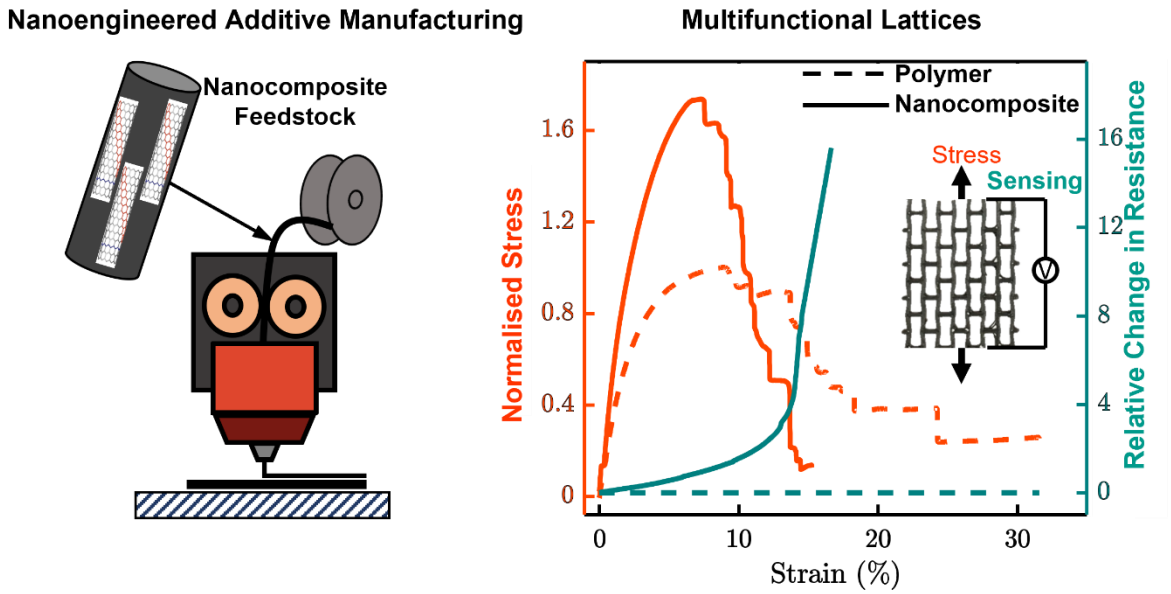

Figures

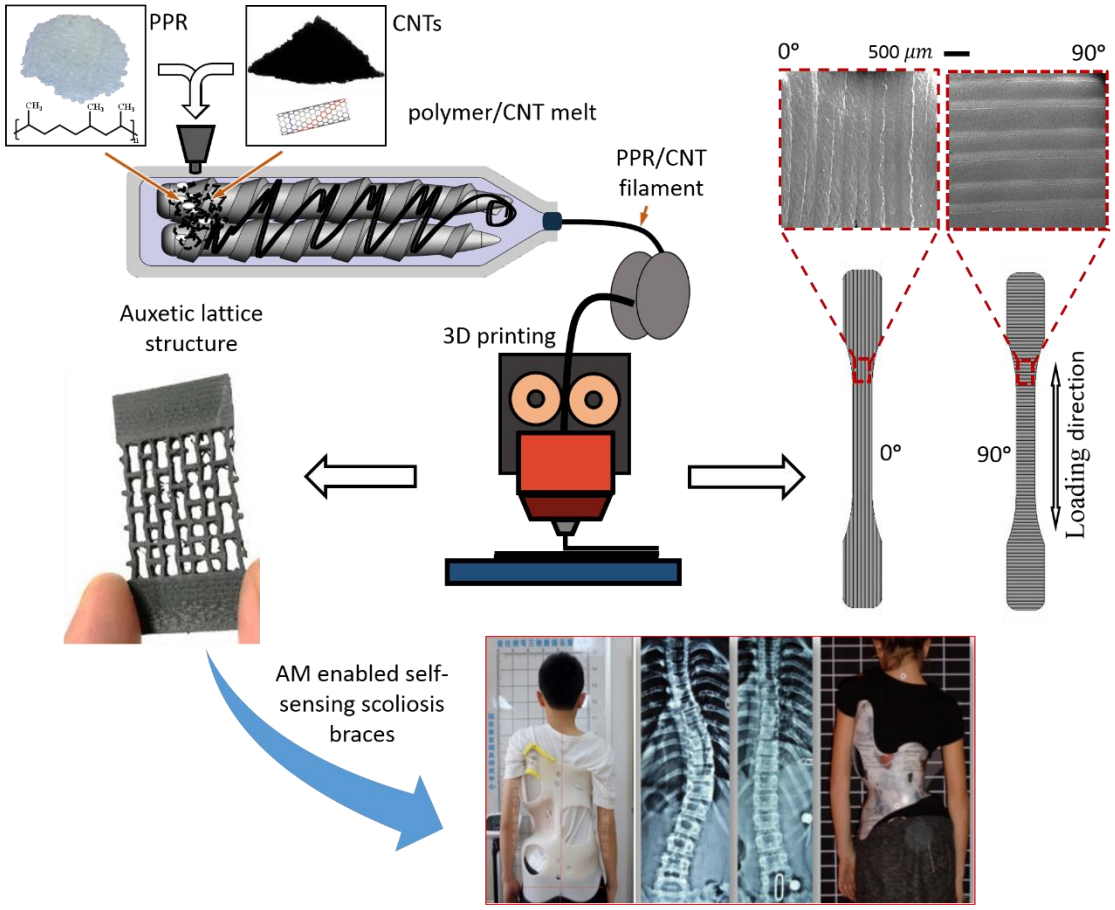

Figure 1. Feedstock filament fabrication (via extrusion) and fused filament fabrication (FFF) of polypropylene random copolymer (PPR)/carbon nanotube (CNT) nanocomposites. 3D printed dogbone specimens (two print-directions) and auxetic lattice structure shown are for testing piezoresistive behavior and development of individually tailored biomedical devices, such as scoliosis braces. Inset from[43].

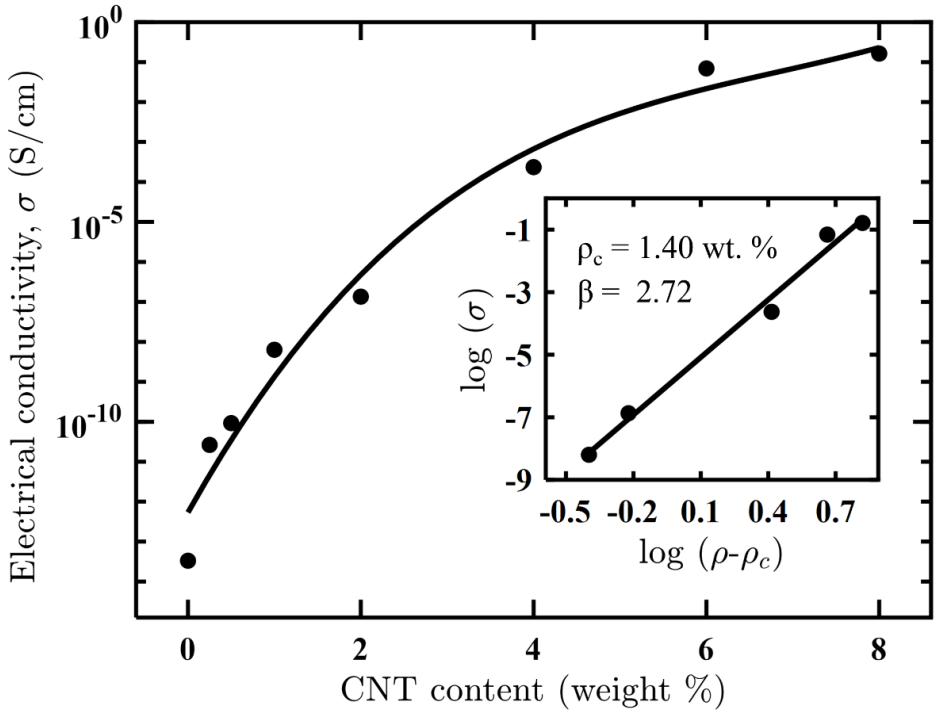

Figure 2. Plot of electrical conductivity (σ) versus CNT content (wt. %) for FFF-printed PPR/CNT composites. Inset shows the log-log plot of σ as a function of $(\rho - \rho_c)$, giving a percolation threshold $\rho_c = 1.4$ wt. %, where ρ is CNT wt. % and β is the critical exponent.

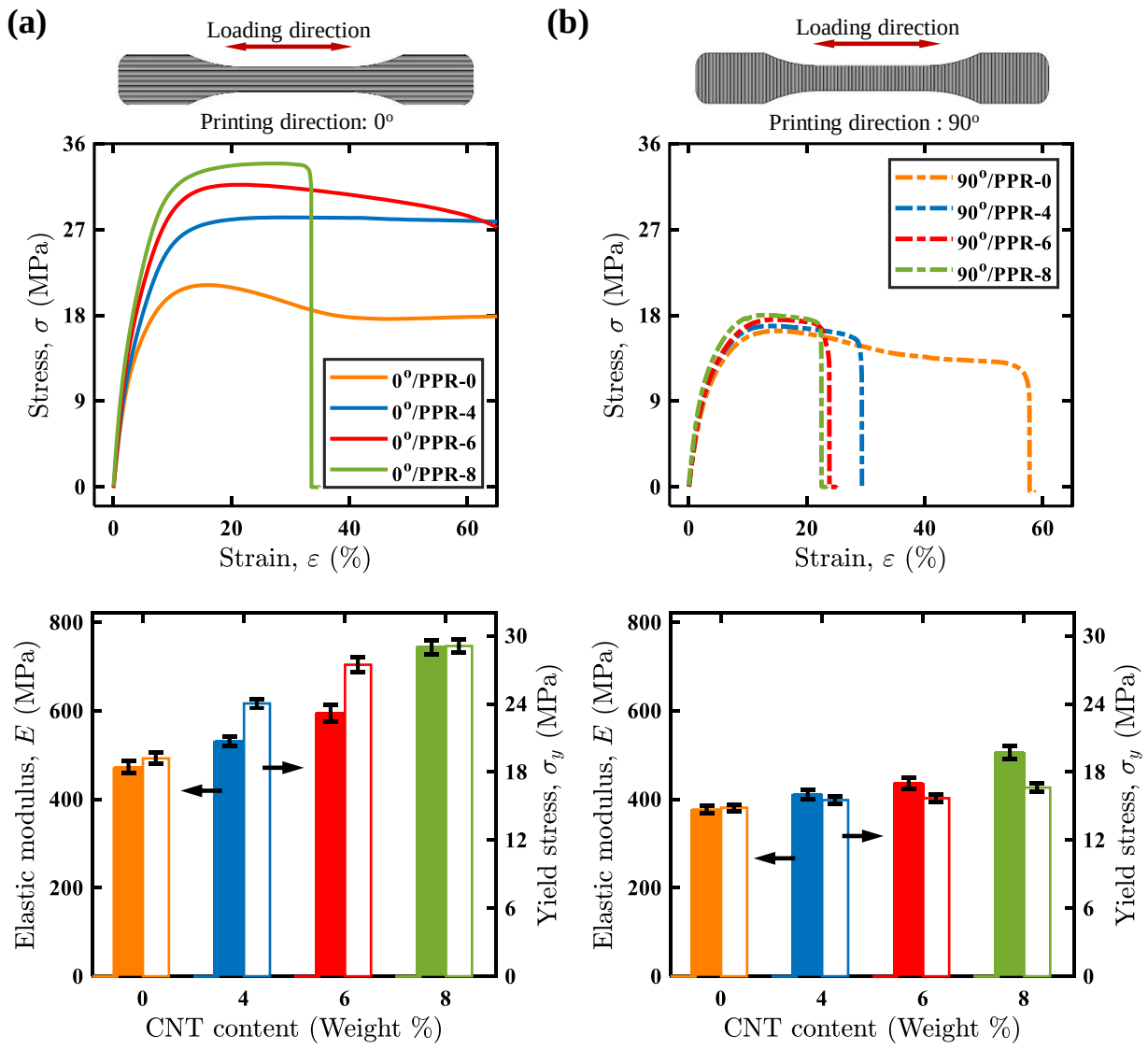

Figure 3. Mechanical response of FFF-enabled PPR/CNT dogbone specimens: (a) and (b) show representative stress-strain response and bar charts of elastic modulus and yield stress as a function of CNT loading for PPR/CNT nanocomposites printed in 0° and 90° directions, respectively.

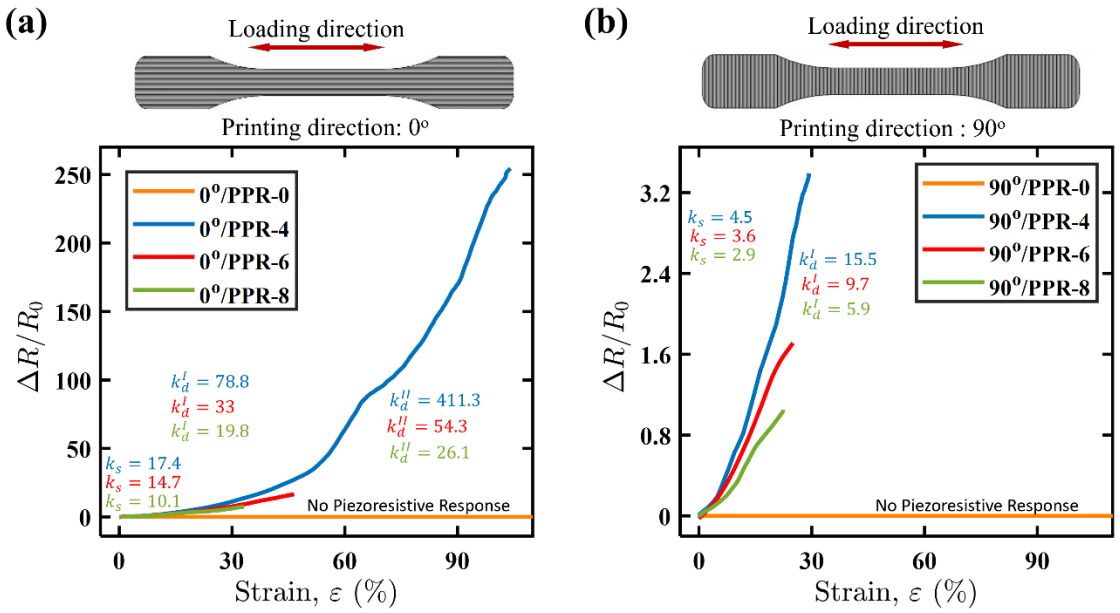

Figure 4. Piezoresistive response of FFF-enabled PPR/CNT dogbone specimens: (a) and (b) show resistance change with strain for composites printed in 0° and 90° directions, respectively. Piezoresistive strain sensitivity, k_s is calculated before yield and damage sensitivity, k_d^I and k_d^{II} is calculated post-yield.

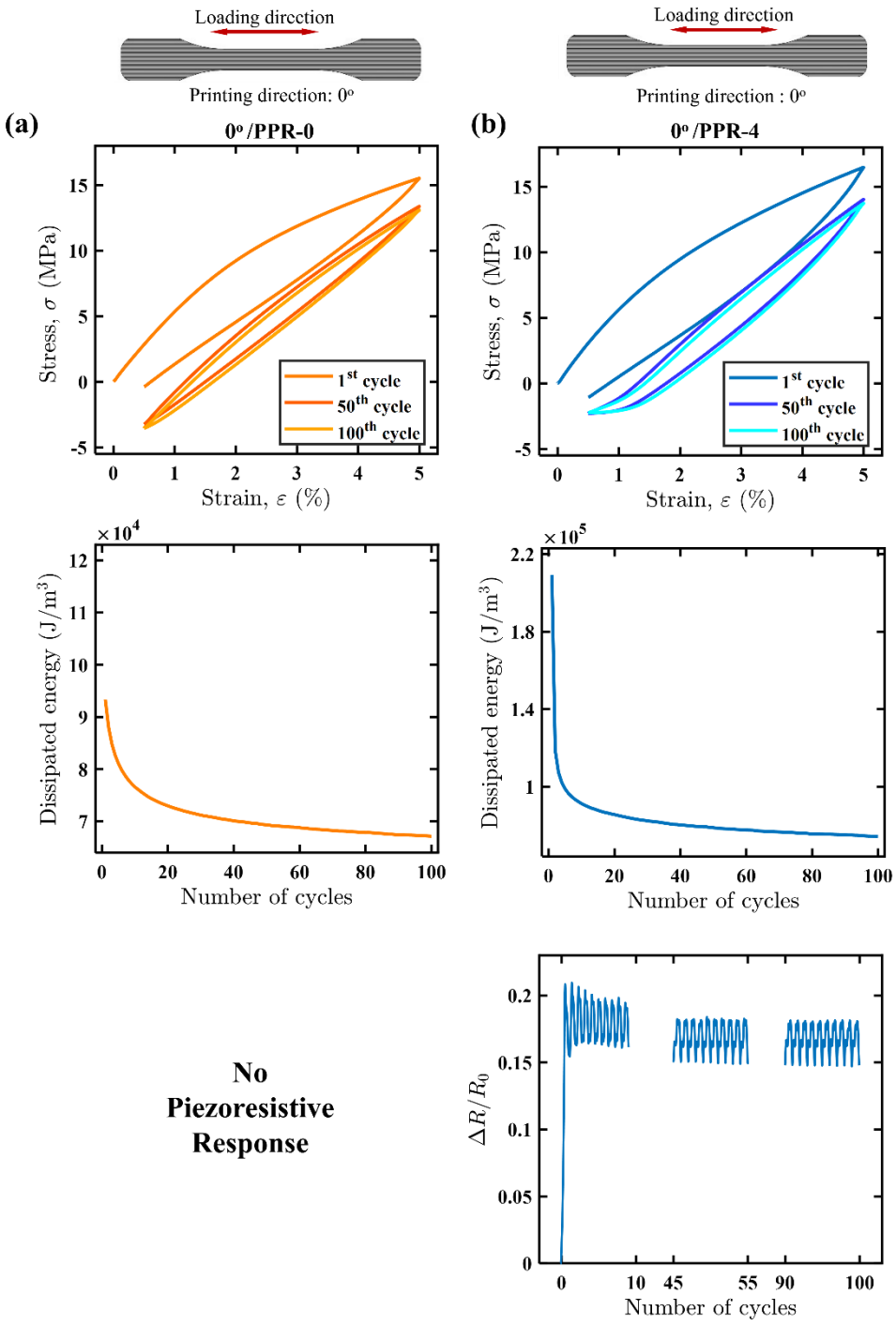

Figure 5. Cyclic loading and unloading (up to 100 cycles) response of PPR and PPR/CNT nanocomposites (comprising 4 wt. % CNT loading) printed in 0° direction: (a) displays the stress-strain curve at 1st, 50th and 100th cycle and dissipated energy per cycle for the PPR-0 samples and (b) displays the stress-strain curve at 1st, 50th and 100th cycle, dissipated energy per cycle and normalized resistance change evolution as a function of number of cycles for the PPR-4 sample**s.**

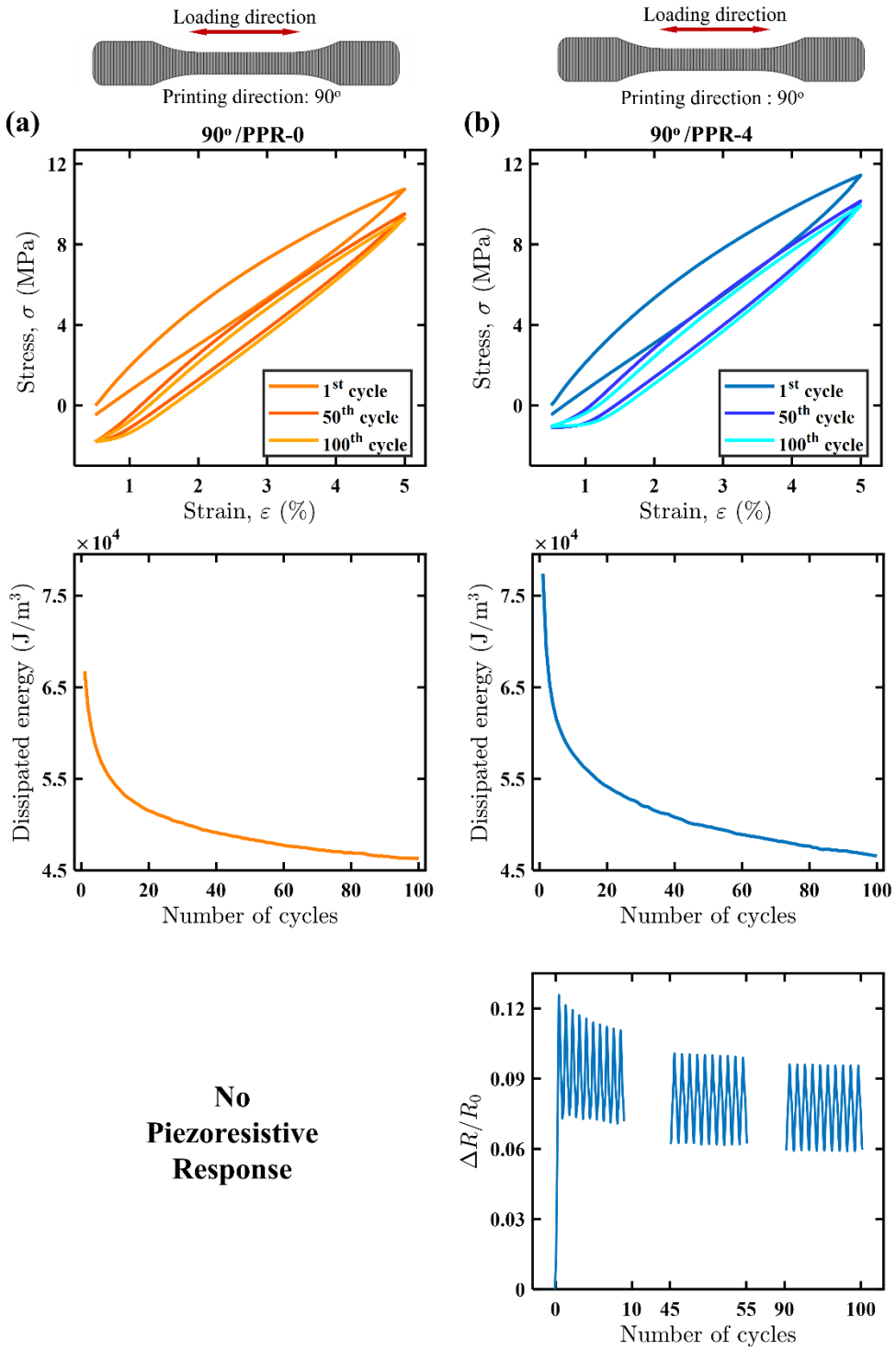

Figure 6. Cyclic loading and unloading (up to 100 cycles) response of PPR and PPR/CNT nanocomposites (having 4 wt. % CNTs loading) printed in 90° direction: (a) displays the stress-strain curve at 1st, 50th and 100th cycle and dissipated energy per cycle for the PPR-0 samples and (b) displays the stress-strain curve at 1st, 50th and 100th cycle, dissipated energy per cycle and normalized resistance change with respect to number of cycles for the PPR-4 samples.

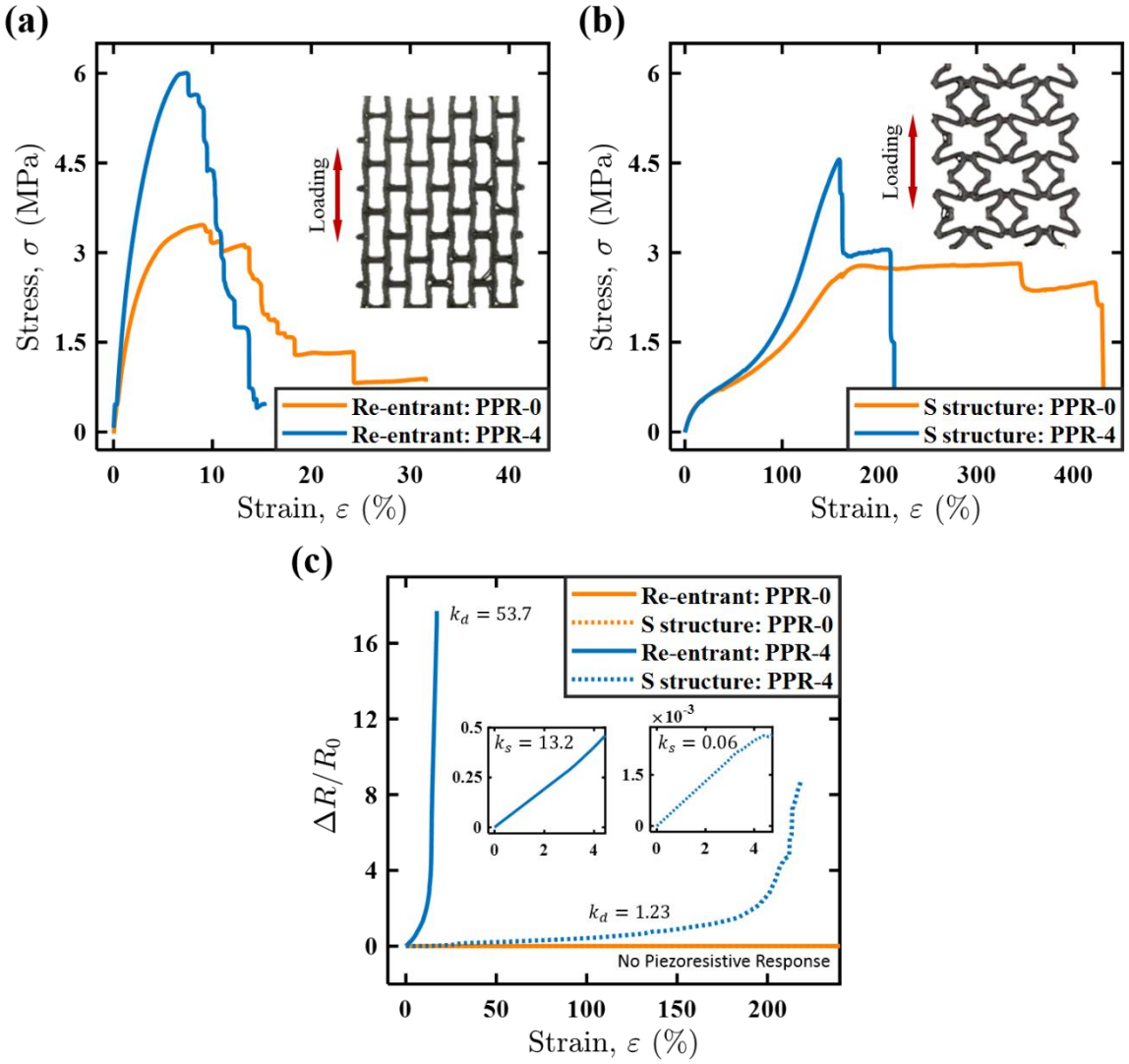

Figure 7. Mechanical and piezoresistive response of PPR/CNT-4 nanocomposite auxetic lattice structures comprising 4wt. % CNT: (a) stress-strain response of re-entrant structure, (b) stress-strain response of S-unit cell structure and (c) piezoresistive response of re-entrant and re-entrant and S-unit cell structures. k_s is calculated before yield and damage sensitivity, k_d^l is calculated post-yield.

Table 1. Mechanical response of FFF-enabled PPR/CNT dog-bone samples: Elastic modulus, yield strain, yield stress, tensile strength, failure strain and modulus of toughness with CNT loading of PPR/CNT nanocomposites in 0^o printing direction. Standard errors as well as % change from PPR-0 baseline response, where statistically significant are indicated.

Sample Type	Elastic modulus (MPa)	Yield strain (%)	Yield stress (MPa)	Tensile strength (MPa)	Failure strain (%)	Modulus of toughness (10^3 J/mm^3)
0^o/PPR-0	476± 14 $\varepsilon \leq 3.92\%$	8.02 ± 0.12	19.2± 0.46	21.17±2.87	802 ± 140	157.21± 36
0^o/PPR-4	531± 11 $\varepsilon \leq 4.02\%$ (+12.7%)	8.52 ± 0.17 (+6.2%)	24.04±0.54 (+25%)	28.27± 1.2 (+33%)	124 ± 4 (-84%)	32.42± 2.7 (-79%)
0^o/PPR-6	594± 19 $\varepsilon \leq 4.1\%$ (+25.9%)	8.62 ± 0.16 (+7.4%)	27.45±0.66 (+42%)	31.7± 1.01 (+49%)	72 ± 1.1 (-91%)	20.21± 0.4 (-87%)
0^o/PPR-8	743± 16 $\varepsilon \leq 4.12\%$ (+56.4%)	8.79 ± 0.09 (+9.6%)	29.1± 0.49 (+52%)	33.9± 1.2 (+60%)	35 ± 0.5 (-95%)	9.98± 0.2 (-93%)

Table 2. Mechanical response of FFF-enabled PP-CNT dog-bone specimens: Elastic modulus, yield strain, yield stress, tensile strength, failure strain and modulus of toughness for different PPR/CNT nanocomposites printed in 90^o direction. Standard errors as well as % change from PPR-0 baseline response, where statistically significant are indicated.

Sample designation	Elastic modulus (MPa)	Yield strain (%)	Yield stress (MPa)	Tensile strength (MPa)	Failure strain (%)	Modulus of toughness (10^3 J/mm^3)
90^o/PPR-0	377± 9 $\varepsilon \leq 3.14\%$	7.28 ± 0.11	14.86±0.29	16.36±1.22	58 ± 0.2	8± 0.1
90^o/PPR-4	410± 11 $\varepsilon \leq 3.23\%$ (+9%)	7.42 ± 0.08 (+1.9%)	15.52± 0.3 (+5%)	16.88±0.87 (+3%)	29 ± 0.1 (-50%)	4.35 ± 0.03 (-45%)
90^o/PPR-6	437± 12 $\varepsilon \leq 3.24\%$ (+16%)	7.39 ± 0.21 (+1.5%)	15.69±0.35 (+6%)	17.56±0.93 (+7%)	25 ± 0.1 (-56%)	3.57± 0.04 (-55%)

90°/PPR-8	506± 16 $\varepsilon \leq 3.27\%$ (+34%)	7.55 ± 0.17 (+3.7%)	16.62±0.39(+12%)	18.02±0.66(+10%)	23 ± 0.1 (-60%)	3.52± 0.04 (-56%)

Table 3. Piezoresistive response of FFF-enabled PPR/CNT dog-bone specimens printed in 0° direction: Strain sensitivity and damage sensitivity are summarized.

Sample designation	Strain Sensitivity, k_s $(\Delta R/R_0)$	Damage Sensitivity, k_d^I $(\Delta R/R_0)$	Damage Sensitivity, $k_d^{II}(\Delta R/R_0)$
0°/PPR-4	17.4, $0 \leq \varepsilon \leq 8.52\%$	78.8, $8.52\% \leq \varepsilon \leq 51\%$	411.3, $51\% \leq \varepsilon \leq 104\%$
0°/PPR-6	14.7, $0 \leq \varepsilon \leq 8.62\%$	33, $8.62\% \leq \varepsilon \leq 30\%$	54.29, $30\% \leq \varepsilon \leq 46.5\%$
0°/PPR-8	10.1, $0 \leq \varepsilon \leq 8.79\%$	17.8, $8.79\% \leq \varepsilon \leq 15\%$	26.1, $15\% \leq \varepsilon \leq 33.2\%$

Table 4. Piezoresistive response of FFF-enabled PPR/CNT dog-bone specimen printed in 90° direction: Strain sensitivity and damage sensitivity are summarized.

Sample designation	Strain Sensitivity, k_s $(\Delta R/R_0)$	Damage Sensitivity, k_d^I $(\Delta R/R_0)$
90°/PPR-4	4.5, $0 \leq \varepsilon \leq 7.42\%$	15.5, $7.42\% \leq \varepsilon \leq 30\%$
90°/PPR-6	3.6, $0 \leq \varepsilon \leq 7.39\%$	9.7, $7.39\% \leq \varepsilon \leq 25\%$
90°/PPR-8	2.9, $0 \leq \varepsilon \leq 7.55\%$	5.9, $7.55\% \leq \varepsilon \leq 21.6\%$

Table 5. Mechanical response of FFF-printed auxetic lattice structures using PPR-0 and PPR-4: Elastic modulus, strength, modulus of toughness and failure strain are summarized.

Sample designation		Elastic Modulus (MPa)	Strength (MPa)	Modulus of Toughness (10^3 J/mm^3)	Failure Strain (%)
Re-entrant	PPR-0	154 $\varepsilon \leq 1.01\%$	3.46	0.62	14.56%
	PPR-4	233 $\varepsilon \leq 0.99\%$ (+51.2%)	5.99 (+73.1%)	0.55 (-11.3%)	9.04% (-37.9%)
S-structure	PPR-0	3.9 $\varepsilon \leq 3.72\%$	2.78	9.22	429%
	PPR-4	4.5 $\varepsilon \leq 3.70\%$ (+15.4%)	4.54 (+63.3%)	3.01 (-67%)	211% (-50.8%)

Table 6. Piezoresistive response of FFF-printed auxetic structures using PPR-4: Strain sensitivity and damage sensitivity are summarized

Sample designation		Strain Sensitivity, k_s $(\Delta R/R_0)$	Damage Sensitivity, k_d $(\Delta R/R_0)$
Re-entrant	PPR-4	13.2, $0\% \leq \varepsilon \leq 4.45\%$	53.7, $4.45\% \leq \varepsilon \leq 14.1\%$
S-structure	PPR-4	0.06, $0\% \leq \varepsilon \leq 4.73\%$	1.23, $4.73\% \leq \varepsilon \leq 196\%$